THE JOURNAL OF PHYSICAL CHEMISTRY Letters

Letter

Cite This: J. Phys. Chem. Lett. 2018, 9, 6709−6715

pubs.acs.org/JPCL

Screening Magnetic Two-Dimensional Atomic Crystals with Nontrivial Electronic Topology

Hang Liu,[†,§] Jia-Tao Sun,*[,†,§] Miao Liu,[†] and Sheng Meng*[,†,‡,§]

[†]Beijing National Laboratory for Condensed Matter Physics and Institute of Physics, Chinese Academy of Sciences, Beijing 100190, People's Republic of China

[‡]Collaborative Innovation Center of Quantum Matter, Beijing 100190, People's Republic of China

[§]University of Chinese Academy of Sciences, Beijing 100049, People's Republic of China

Supporting Information

ABSTRACT: To date, only a few two-dimensional (2D) magnetic crystals have been experimentally confirmed, such as CrI_3 and $CrGeTe_3$, all with very low Curie temperatures (T_C). High-throughput first-principles screening over a large set of materials yields 89 magnetic monolayers including 56 ferromagnetic (FM) and 33 antiferromagnetic compounds. Among them, 24 FM monolayers are promising candidates possessing T_C higher than that of CrI_3. High T_C monolayers with fascinating electronic phases are identified: (i) quantum anomalous Hall and valley Hall effects coexist in a single material $RuCl_3$ or VCl_3, leading to a valley-polarized quantum anomalous Hall state; (ii) $TiBr_3$, Co_2NiO_6, and $V_2H_3O_5$ are revealed to be half-metals. More importantly, a new type of fermion dubbed type-II Weyl ring is discovered in ScCl. Our work provides a database of 2D magnetic materials, which could guide experimental realization of high-temperature magnetic monolayers with exotic electronic states for future spintronics and quantum computing applications.

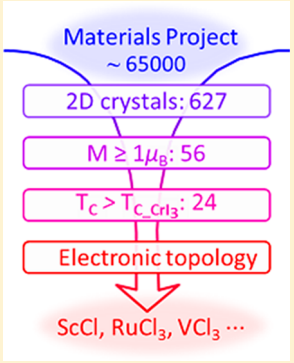

The discovery of two-dimensional (2D) materials opens a new avenue with rich physics promising for applications in a variety of subjects including optoelectronics, valleytronics, and spintronics, many of which benefit from the emergence of Dirac/Weyl fermions. One example is transition-metal dichalcogenide (TMDC) monolayers, whose finite direct bandgaps enable novel optoelectronic controls as well as valley-dependent phenomena, such as circular dichroism and the valley Hall effect (VHE).[1,2] Due to the equivalent occupation of K and K′ valleys in TMDC materials, the VHE does not produce observable macroscopic Hall voltage. This is overcome in magnetic counterparts, resulted from time reversal symmetry breaking.[3−8] In contrast to fermions in nonmagnetic systems, such as massless Dirac fermions in borophene, black phosphorus, and Cu_2Si[9−13] and massive Dirac fermions in graphene and bilayer bismuth,[14,15] few types of fermions in 2D magnetic systems are proposed, implying the scarcity of intrinsic magnetic 2D crystals. In particular, 2D magnets with massive Dirac fermions can support the quantum anomalous Hall state leading to topologically protected spin current, promising for low-power-consumption devices. Unfortunately, the state is only realized in 2D materials with nonintrinsic magnetism at extremely low temperature (e.g., 30 mK for Cr-doped $(Bi,Sb)_2Te_3$ thin film),[16−22] hampering its extensive applications. Therefore, discovery of 2D magnets at an elevated temperature is of great importance, providing optimal platforms to enable realistic spintronic and quantum devices, as well as to realize new electronic states.

The Mermin−Wagner theorem shows that the 2D isotropic Heisenberg model prohibits the occurrence of 2D magnetic order,[23] while this restriction is removed by magnetic anisotropy, possibly leading to 2D Ising magnetism.[24] To date, 2D magnetic materials are limited to marginal modifications to existing compounds, for instance by (i) adsorbing hydrogen on graphene,[25] (ii) reconstructing surface/edge,[26,27] or (iii) creating defects in MoS_2 nanosheets.[28] The intrinsic 2D ferromagnetism has only been observed in atomically thin CrI_3 and $CrGeTe_3$, only accessible at a low temperature of ∼40 K.[29,30] The absence of ideal 2D magnetic materials indicates that traditional trial-and-error approaches to discover new materials are not effective. Recently, computational screening from existing material databases presents an essential tool to accelerate materials discovery.[31−40] Hence, the big challenge to identify monolayer magnets may be addressed by high-throughput calculations based on density functional theory.

In this work, we employ high-throughput first-principles calculations to systematically screen monolayer materials with intrinsic magnetism at a high temperature, better if they are equipped with nontrivial topological properties. We have successfully identified 56 ferromagnetic (FM) monolayers, including 24 monolayers with a Curie temperature (T_C) higher than that of monolayer CrI_3. We also find that the quantum anomalous Hall and valley Hall effect coexist in FM monolayers of VCl_3 and $RuCl_3$, supporting the native existence

Received: September 10, 2018
Accepted: November 7, 2018
Published: November 7, 2018

DOI: 10.1021/acs.jpclett.8b02783
J. Phys. Chem. Lett. 2018, 9, 6709−6715

of valley-polarized, topologically protected, quantized spin current. Monolayer ScCl possesses 2D type-II Weyl nodal ring centering on the Γ point, which may lead to intriguing electronic properties beyond known fermions. Our work provides a rich data set of materials potentially supporting high-temperature 2D magnetism as well as new topological states.

The computational screening process is schematically shown in Figure 1. We start from a 2D materials database obtained by screening Materials Project data (with ~65 000 entries) using the topology-scaling algorithm.[31] As shown in Figure 2a, 627 monolayer materials, including 7 unary, 220 binary, 323 ternary, 69 quaternary, and 8 quinary 2D compounds, have the exfoliation energy below that of the experimentally existing SnSe monolayer (150 meV/atom).[31] To investigate their magnetic properties, spin-polarized calculations with collinear magnetic configurations are carried out, where the initial magnetic moment is set as 6 μ_B for each magnetic atom. Only materials with the final magnetic moment larger than 1 μ_B/unit cell are selected as 2D magnetic candidates for further computation. This screening process yields 89 magnetic monolayers, including 33 binary, 39 ternary, 13 quaternary, and 4 quinary compounds. As shown in Figure 2b. It is clear that ternary compounds top the list, followed by binary, quaternary, and quinary compounds. All magnetic monolayers contain transition-metal (TM) atoms, indicating that the design of magnetic monolayers should be restricted to TM-containing materials.

The purpose of this work is to identify the *candidates* of 2D magnetic crystals through large-scale screening of known materials, rather than to provide the most accurate prediction of a specific magnetic material. To be practical for the large-scale screening, all magnetic calculations are based on PBE functionals without orbital-dependent on-site Coulomb (U) and exchange interactions (J), which may play an important role in predicting accurate magnetic properties for transition-metal oxides.[41−45] The comparisons between our results and previous works using more accurate functionals and $U-J$

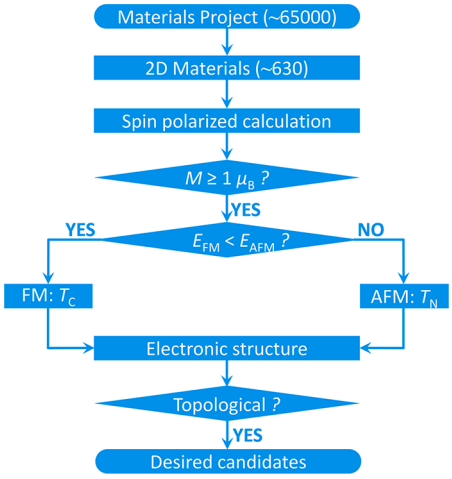

Figure 1. Flowchart of computational high-throughput screening.

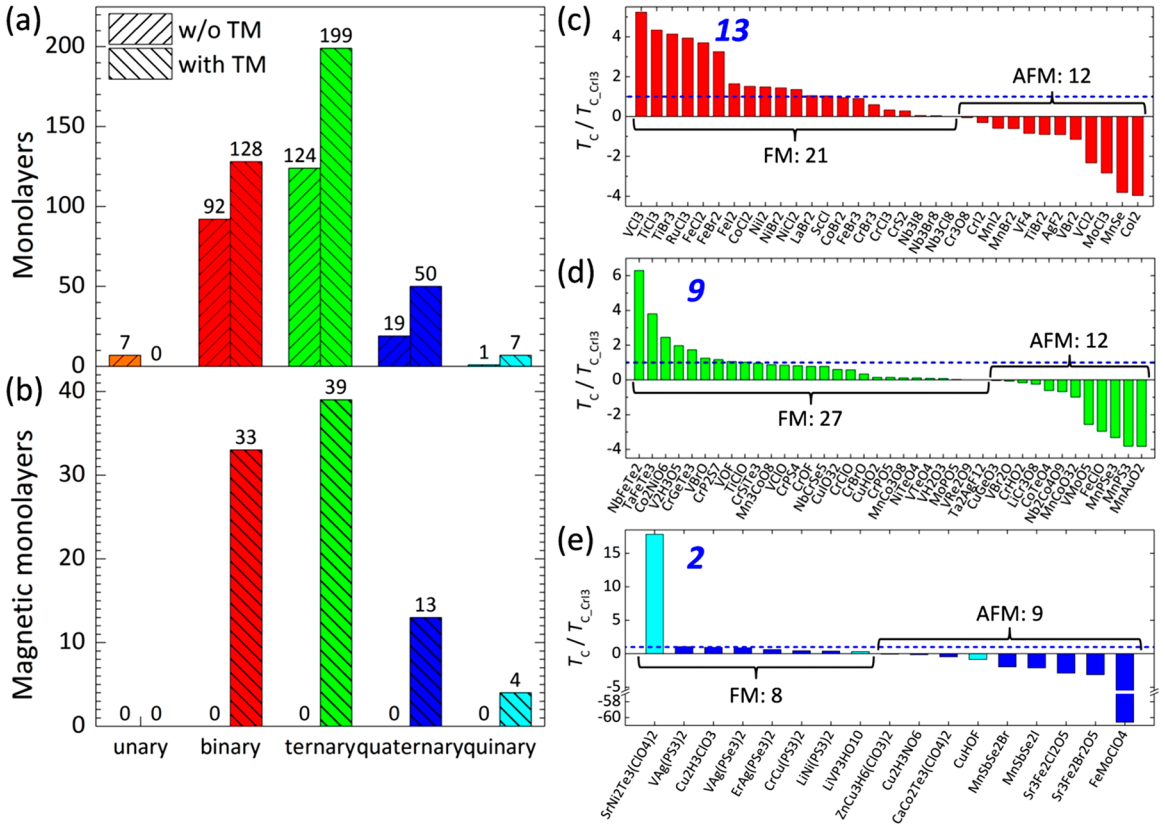

Figure 2. Screened magnetic monolayer materials. (a) The initial 627 monolayer materials are classified as unary (orange), binary (red), ternary (green), quaternary (blue), and quinary (cyan). Every classification is classified further according to whether it contains TM atoms or not. (b) Classification of 89 magnetic monolayers with magnetic moment larger than 1 μ_B/unit cell. Curie temperature of magnetic binary (c), ternary (d), quaternary, and quinary (e) monolayers.

DOI: 10.1021/acs.jpclett.8b02783
J. Phys. Chem. Lett. 2018, 9, 6709−6715

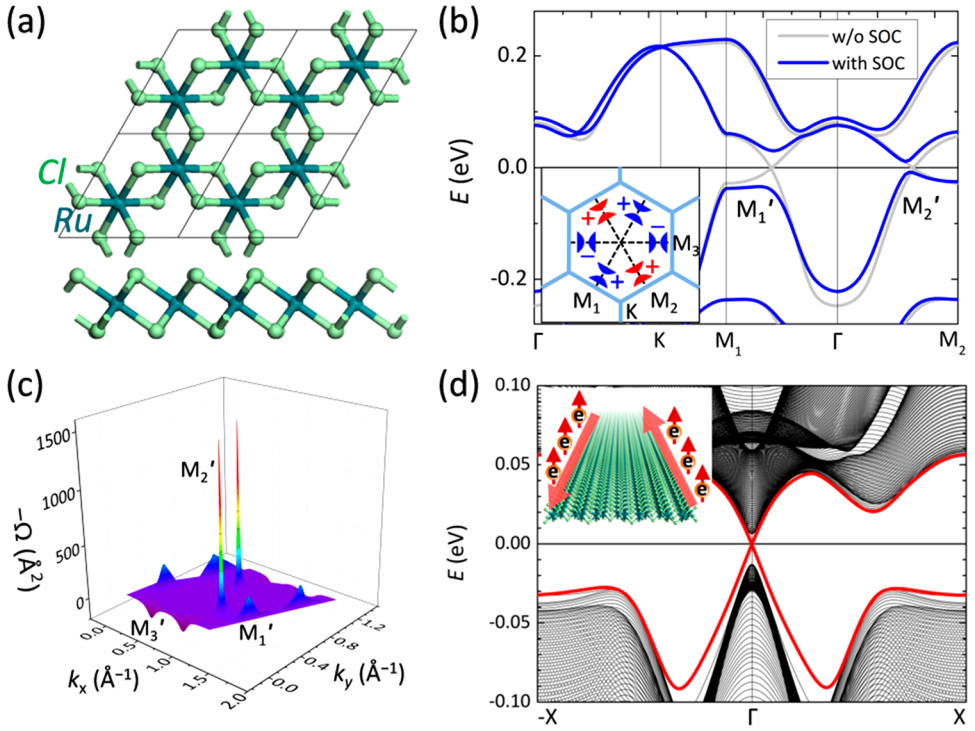

Figure 3. Quantum anomalous Hall state in ferromagnetic monolayer $RuCl_3$. (a) Atomic structure of $RuCl_3$. (b) Band structure of $RuCl_3$ with (blue line) and without SOC (gray line). The inset shows all the massive Dirac cones and corresponding sign of Berry curvature. (c) Berry curvature in FBZ. (d) Band structure of $RuCl_3$ nanoribbon with a width of 386 Å. The red line shows the topologically protected edge states. The inset shows the quantized spin current on two edges.

corrections show that[46−51] the simplified first-principles approach adopted here may give a rough, yet proper, account of electronic structures for the purpose of large-scale screening of magnetic monolayer crystals (see details in Supporting Information). This rough estimation serves as the first step for finding perfect 2D magnetic materials, which are subject to future experimental tests or more advanced theoretical calculations.

To determine magnetic ground state, the total energy of antiferromagnetic (AFM) state (E_{AFM}) is compared with that of the FM state (E_{FM}). With regard to the magnetic structure of the AFM state, the checkerboard configuration is adopted preferentially, which is also used for obtaining the Curie/Néel temperature by mean field approximation. When the self-consistence convergence of computation fails for the checkerboard case, the stripe configuration is also considered (see Figure S1 for details about magnetic configurations). As shown in Figure 2c−e, there are 56 (33) FM (AFM) monolayers, consisting of 21 (12) binary, 27 (12) ternary, 6 (7) quaternary, and 2 (2) quinary compounds. Binary FM monolayers are mostly halides, while chalcogenides dominate ternary magnetic monolayers. The magnetic monolayers can be further classified by their structural prototypes. Binary magnetic compounds mainly include the prototypes with compositions XY_2 and XY_3, possessing space groups $P\bar{3}m1$ and $P\bar{3}1m$, respectively. Anions therein belong to the VI A and VII A groups of elements, and cations are mostly from the TMs in the fourth and fifth element rows. Unlike the binaries, there are rich structural prototypes for ternary compounds, which can be used as prototypes to extend the candidate list to a larger compositional space by atomic substitution. This candidate list also serves as guidance toward experimental synthesis of FM and AFM monolayers, whose phase stability can be examined by comparing the energies of nonmagnetic, FM, and AFM states as shown in Tables S1, S2, and S3.

Next, the Curie (Néel) temperature T_C (T_N) is calculated to give the upper limit of the transition temperature of screened FM (AFM) monolayers. The critical transition temperature of ferromagnets T_C and antiferromagnets T_N in the mean field approximation is calculated by[52−55]

$$E_{AFM} - E_{FM} = N\frac{3}{2}k_B T_{C(N)} \quad (1)$$

where E_{FM} and E_{AFM} are the total energy of magnetic monolayers with N magnetic atoms in ferromagnetic and antiferromagnetic states, respectively. Here k_B denotes the Boltzmann constant. The critical transition temperature of the 89 magnetic monolayers is shown in Figure 2c−e, as grouped by the number of atomic species. The T_C of CrX_3 ($CrXTe_3$) monolayers decreases as element X is replaced by I, Br, and Cl (Ge, Si) successively, which is consistent with Monte Carlo simulations.[47,51] This indicates that, although the absolute value of $T_{C(N)}$ in eq 1 is a rough estimation, the qualitative comparison between different materials is reasonable. In the same spirit, the calculated $T_{C(N)}$ from mean field approximation (MFA) is corrected by rescaling $\frac{T_{C(N)\_cor}}{T_{C(N)}} = \frac{T_{C\_exp}|_{CrI3}}{T_C|_{CrI3}}$, where $T_{C(N)\_cor}$ is the corrected value, and $T_{C\_exp}|_{CrI3} = 45$ K is the experimental T_C of CrI_3.[29] The T_C under MFA can be further corrected by Ising model analysis,[56,57] leading to a more accurate value for the Curie temperature (see Table S4 for details).

Similar to previous reports on engineering T_C by atomic substitution in CrX_3 and $CrXTe_3$ monolayers,[47,51] new materials supporting the same behaviors have been identified. When the chemical element is changed from Cl to Br to I

DOI: 10.1021/acs.jpclett.8b02783
J. Phys. Chem. Lett. 2018, 9, 6709−6715

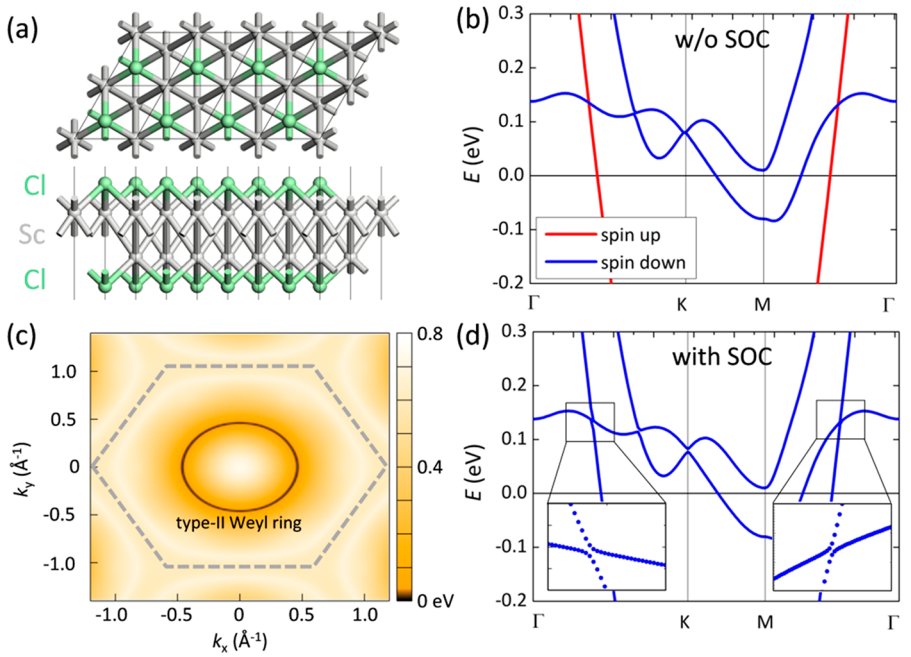

Figure 4. 2D type-II Weyl ring in ferromagnetic monolayer ScCl. (a) Atomic structure of monolayer ScCl. (b) Band structure without SOC. Band structure with SOC (d) and location of type-II Weyl ring (c).

successively, T_C in FM monolayers of NiX_2, VX_2, and MnX_2 increases gradually. In contrast, this behavior in systems of FeX_2 and CoX_2 is reversed. Specifically, the T_C of CoX_2 decreases so significantly that it becomes a negative value for CoI_2, manifesting the change from the FM state in $CoCl_2$ and $CoBr_2$ to the AFM state in CoI_2. Along with this transition of magnetic order, the electronic structure changes from semiconducting in $CoCl_2$ and $CoBr_2$ to metallic in CoI_2. Hence, phase transitions between FM (semiconducting) and AFM (metallic) states can be realized by doping iodine atoms in $CoCl_2$ or $CoBr_2$, offering an alternative way to engineer magnetism.[58,59]

The Curie temperature of the FM CrI_3 monolayer ($T_C|_{CrI3}$ = 290 K) is taken as a reference to screen high-temperature 2D magnets. As shown in Figure 2c–e, we identified 24 FM monolayers, including 13 binary, 9 ternary, 1 quaternary, and 1 quinary compounds, to have T_C higher than that of CrI_3. This implies that the FM order in these materials can be observed at a higher temperature than that of CrI_3. Among them, new semiconductors ($CoCl_2$, NiI_2, $NiBr_2$, $NiCl_2$, $LaBr_2$, $CrGeTe_3$, and CrP_2S_7), new semimetals (VCl_3, $RuCl_3$, and ScCl), new half-metals ($TiBr_3$, Co_2NiO_6, and $V_2H_3O_5$), and new metals ($NbFeTe_2$ and $TaFeTe_3$) are proposed (see Figures S2, S3, and S4 for details). Besides binary and ternary compounds, monolayers with more types of chemical elements are also promising candidates for 2D spintronic applications. For example, the T_N of $FeMoClO_4$ is 60 times higher than T_{C_CrI3}, suggesting a great potential for use in realistic devices.

Because of time reversal symmetry breaking, magnetic monolayers identified above may host topologically nontrivial physics. Monolayer $RuCl_3$ exhibits $T_C = 4.0 \times T_C|_{CrI3}$, and each Ru atom possesses an in-plane anisotropic magnetic moment of 1 μ_B with $S_y - S_x = 0.008$ μ_B (Figure 3a), which is quite different from the magnetic ground state with zigzag AFM order[60−62] and field-induced spin liquid state[63−66] in three-dimensional bulk $RuCl_3$. The out-of-plane and in-plane magnetic anisotropy energies, with $E[100] - E[001] = -19$ meV and $E[100] - E[010] = 61$ μeV,[49] respectively, also demonstrate the occurrence of ferromagnetic order in monolayer $RuCl_3$. It should be noted that the predicted ferromagnetic state of monolayer $RuCl_3$ can be changed because of the lack of the on-site U term and exchange interaction J term. When spin−orbit coupling (SOC) is not considered, there are six spin-polarized massless Dirac cones along the ΓM path, shown in Figure 3b. When SOC is considered, all the massless Dirac cones become massive, leading to four valleys with band gaps of 64 meV (M_1', M_3') and two valleys with band gaps of 19 meV (M_2'). These energy gaps obtained from calculations with the pure PBE functional can be further corrected by using more accurate functionals and U−J corrections. To further characterize the insulating state, we calculate the Chern number $C = \frac{1}{2\pi}\sum_n \int_{BZ} d^2k\ \Omega_n$. The momentum-space Berry curvature Ω_n for the nth band is given by[22,67]

$$\Omega_n(k) = -\sum_{n' \neq n} \frac{2\ \mathrm{Im}\langle \Psi_{nk}|\hat{v}_x|\Psi_{n',k}\rangle\langle \Psi_{n',k}|\hat{v}_y|\Psi_{nk}\rangle}{(E_{n'} - E_n)^2} \quad (2)$$

where n and n' are band indexes and $\hat{v}_x$ and $\hat{v}_y$ are velocity operators along the x and y directions. As shown in Figure 3b,c, the sign of the Berry curvature around the M_3' valley is opposite to that of the M_1' and M_2' valleys, leading to opposite anomalous velocities of electrons from M_3' and M_1', M_2' valleys under the in-plane electric field. This phenomenon is known as VHE.[68] Specifically, natively measurable valley Hall voltage appears, resulted from inequivalent numbers of valley electrons with positive and negative Berry curvatures.

Integrating the Berry curvature in the first Brillouin zone (FBZ) leads to nonzero Chern number $C = -1$, indicating that FM monolayer $RuCl_3$ exhibits QAHE. The calculated Chern number is consistent with the band structure of $RuCl_3$ nanoribbon with a width of 386 Å, where there is one quantized spin-polarized conductance channel protected from scattering on each edge (Figure 3d). Compared with previous

DOI: 10.1021/acs.jpclett.8b02783
J. Phys. Chem. Lett. 2018, 9, 6709−6715

works to realize QAHE by magnetic doping[17] or functionalizing 2D materials,[20,69] the valley-polarized QAHE (v-QAHE) emerges in intrinsic magnetic $RuCl_3$ at high temperature, much easier to be realized in experiments and utilized in devices. Besides, the coexistence of intrinsic QAHE and natively polarized VHE in monolayer $RuCl_3$ indicates that it is a good platform to study the interplay between QAHE and VHE. Similarly, monolayer VCl_3 with $C = 1$ also supports the v-QAHE (see details in Figure S5). However, in contrast with the completely in-plane magnetic moment of $RuCl_3$, the magnetic moment of VCl_3 has an out-of-plane component, which is promising for hosting intriguing noncollinear and noncoplanar spin chirality.[70]

Besides the superior materials to realize already-known states, a new electronic state is also identified. The FM monolayer ScCl, with a magnetic moment of 1.5 μ_B/unit cell and $T_C = 1.03 \times T_C|_{CrI3}$, consists of two chlorine atomic layers intercalated by two scandium atomic layers (see Figure 4a). As shown in Figure 4b,c, spin-up and spin-down bands cross with each other at the energy of 0.13 eV, resulting in a nodal ring around Γ point. Each crossing point on this ring is doubly degenerate, which is different from the quadruple Dirac ring in 2D Cu_2Si.[11] Moreover, because each cone on the ring has type-II band dispersion, it is dubbed a type-II Weyl ring here, which may possess intriguing topologically nontrivial electronic properties. Due to weak SOC of Sc and Cl atoms, the band gap on the ring is negligible, as shown in Figure 4d. This type-II Weyl ring almost occupies half of the FBZ (Figure 4c), leading to easy observation in experiment using, e.g., angle resolved photoemission spectroscopy.

In conclusion, we have identified 89 magnetic monolayers, including 33 binary, 39 ternary, 13 quaternary, and 4 quinary compounds through high-throughput computational screening based on first-principles calculations without including on-site Coulomb and spin−spin interactions. Under the mean field approximation, we find 24 monolayers with T_C potentially higher than that of experimentally confirmed ferromagnet CrI_3. Furthermore, from these high T_C monolayers, new half-metals $TiBr_3$, Co_2NiO_6, and $V_2H_3O_5$ are proposed, and new ferromagnets $RuCl_3$ and VCl_3 are found to support valley-polarized QAHE. Besides, a novel electronic state named type-II Weyl ring is predicted in monolayer ferromagnetic ScCl. Our work provides a significant clue to realize 2D high-temperature ferromagnets with novel Dirac/Weyl fermions. This work may stimulate further investigations on the effect of layer thickness, magnetic configurations, and light-magnetism interaction of these magnetic 2D crystals.

■ ASSOCIATED CONTENT

Supporting Information

The Supporting Information is available free of charge on the ACS Publications website at DOI: 10.1021/acs.jpclett.8b02783.

Computational methods, magnetic configurations, the atomic and electronic structures of semiconducting, metallic, half-metallic 2D magnetic materials with high T_c, data sets of 2D magnetic monolayers for Figure 2, further correciton of the Curie temperature, and the influence of U and J (PDF)

■ AUTHOR INFORMATION

Corresponding Authors

*E-mail: jtsun@iphy.ac.cn (J.T.S.).
*E-mail: smeng@iphy.ac.cn (S.M.).

ORCID

Jia-Tao Sun: 0000-0003-3519-352X
Sheng Meng: 0000-0002-1553-1432

Notes

The authors declare no competing financial interest.

■ ACKNOWLEDGMENTS

This work was financially supported by the National Basic Research Program of China (Grants No. 2016YFA0202300, No. 2016YFA0300902, No. 2015CB921001, No. 2013CBA01600), National Natural Science Foundation of China (Grants No. 11774396 and No. 61306114), "Strategic Priority Research Program (B)" of Chinese Academy of Sciences (Grants No. XDB30000000 and No. XDB07030100).

■ REFERENCES

(1) Lopez-Sanchez, O.; Lembke, D.; Kayci, M.; Radenovic, A.; Kis, A. Ultrasensitive Photodetectors Based on Monolayer MoS_2. *Nat. Nanotechnol.* **2013**, *8*, 497−501.

(2) Batmunkh, M.; Bat-Erdene, M.; Shapter, J. G. Phosphorene and Phosphorene-Based Materials - Prospects for Future Applications. *Adv. Mater.* **2016**, *28*, 8586−8617.

(3) Liu, J.; Hou, W.-J.; Cheng, C.; Fu, H.-X.; Sun, J.-T.; Meng, S. Intrinsic Valley Polarization of Magnetic VSe_2 Monolayers. *J. Phys.: Condens. Matter* **2017**, *29*, 255501.

(4) Sun, J.-T.; Wang, Z.; Meng, S.; Du, S.; Liu, F.; Gao, H. J. Spin-Polarized Valley Hall Effect in Ultrathin Silicon Nanomembrane via Interlayer Antiferromagnetic Coupling. *2D Mater.* **2016**, *3*, 035026.

(5) Smoleński, T.; Goryca, M.; Koperski, M.; Faugeras, C.; Kazimierczuk, T.; Bogucki, A.; Nogajewski, K.; Kossacki, P.; Potemski, M. Tuning Valley Polarization in a WSe_2 Monolayer with a Tiny Magnetic Field. *Phys. Rev. X* **2016**, *6*, 021024.

(6) Marino, E. C.; Nascimento, L. O.; Alves, V. S.; Smith, C. M. Interaction Induced Quantum Valley Hall Effect in Graphene. *Phys. Rev. X* **2015**, *5*, 011040.

(7) Wang, Z.; Mak, K. F.; Shan, J. Strongly Interaction-Enhanced Valley Magnetic Response in Monolayer WSe_2. *Phys. Rev. Lett.* **2018**, *120*, 066402.

(8) Li, Y.; Ludwig, J.; Low, T.; Chernikov, A.; Cui, X.; Arefe, G.; Kim, Y. D.; van der Zande, A. M.; Rigosi, A.; Hill, H. M.; et al. Valley Splitting and Polarization by the Zeeman Effect in Monolayer $MoSe_2$. *Phys. Rev. Lett.* **2014**, *113*, 266804.

(9) Feng, B.; Sugino, O.; Liu, R. Y.; Zhang, J.; Yukawa, R.; Kawamura, M.; Iimori, T.; Kim, H.; Hasegawa, Y.; Li, H.; et al. Dirac Fermions in Borophene. *Phys. Rev. Lett.* **2017**, *118*, 096401.

(10) Kim, J.; Baik, S. S.; Jung, S. W.; Sohn, Y.; Ryu, S. H.; Choi, H. J.; Yang, B.-J.; Kim, K. S. Two-Dimensional Dirac Fermions Protected by Space-Time Inversion Symmetry in Black Phosphorus. *Phys. Rev. Lett.* **2017**, *119*, 226801.

(11) Feng, B.; Fu, B.; Kasamatsu, S.; Ito, S.; Cheng, P.; Liu, C.-C.; Feng, Y.; Wu, S.; Mahatha, S. K.; Sheverdyaeva, P.; et al. Experimental Realization of Two-Dimensional Dirac Nodal Line Fermions in Monolayer Cu_2Si. *Nat. Commun.* **2017**, *8*, 1007.

(12) Gao, L.; Sun, J. T.; Lu, J. C.; Li, H.; Qian, K.; Zhang, S.; Zhang, Y. Y.; Qian, T.; Ding, H.; Lin, X.; et al. Epitaxial Growth of Honeycomb Monolayer CuSe with Dirac Nodal Line Fermions. *Adv. Mater.* **2018**, *30*, 1707055.

(13) Liu, H.; Sun, J.-T.; Cheng, C.; Liu, F.; Meng, S. Photoinduced Nonequilibrium Topological States in Strained Black Phosphorus. *Phys. Rev. Lett.* **2018**, *120*, 237403.

(14) Drozdov, I. K.; Alexandradinata, A.; Jeon, S.; Nadj-Perge, S.; Ji, H.; Cava, R. J.; Andrei Bernevig, B.; Yazdani, A. One-Dimensional

DOI: 10.1021/acs.jpclett.8b02783
J. Phys. Chem. Lett. 2018, 9, 6709−6715

Topological Edge States of Bismuth Bilayers. *Nat. Phys.* **2014**, *10*, 664−669.
(15) Kane, C. L.; Mele, E. J. Quantum Spin Hall Effect in Graphene. *Phys. Rev. Lett.* **2005**, *95*, 226801.
(16) Yu, R.; Zhang, W.; Zhang, H.-J.; Zhang, S.-C.; Dai, X.; Fang, Z. Quantized Anomalous Hall Effect in Magnetic Topological Insulators. *Science* **2010**, *329*, 61−64.
(17) Chang, C.-Z.; Zhang, J.; Feng, X.; Shen, J.; Zhang, Z.; Guo, M.; Li, K.; Ou, Y.; Wei, P.; Wang, L.-L.; et al. Experimental Observation of the Quantum Anomalous Hall Effect in a Magnetic Topological Insulator. *Science* **2013**, *340*, 167−170.
(18) Liu, C. X.; Qi, X. L.; Dai, X.; Fang, Z.; Zhang, S. C. Quantum Anomalous Hall Effect in $Hg_{1-y}Mn_yTe$ Quantum Wells. *Phys. Rev. Lett.* **2008**, *101*, 146802.
(19) Hsu, C.-H.; Fang, Y.; Wu, S.; Huang, Z.-Q.; Crisostomo, C. P.; Gu, Y.-M.; Zhu, Z.-Z.; Lin, H.; Bansil, A.; Chuang, F.-C.; et al. Quantum Anomalous Hall Insulator Phase in Asymmetrically Functionalized Germanene. *Phys. Rev. B* **2017**, *96*, 165426.
(20) Liang, Q.-F.; Zhou, J.; Yu, R.; Wang, X.; Weng, H. Interaction-Driven Quantum Anomalous Hall Effect in Halogenated Hematite Nanosheets. *Phys. Rev. B* **2017**, *96*, 205412.
(21) Fu, H.; Ren, J.; Chen, L.; Si, C.; Qiu, J.; Li, W.; Zhang, J.; Sun, J.; Li, H.; Wu, K.; et al. Prediction of Silicon-Based Room Temperature Quantum Spin Hall Insulator via Orbital Mixing. *Europhys. Lett.* **2016**, *113*, 67003.
(22) Fu, H.; Liu, Z.; Lian, C.; Zhang, J.; Li, H.; Sun, J.-T.; Meng, S. Magnetic Dirac Fermions and Chern Insulator Supported on Pristine Silicon Surface. *Phys. Rev. B* **2016**, *94*, 035427.
(23) Mermin, N. D.; Wagner, H. Absence of Ferromagnetism or Antiferromagnetism in One- or Two-Dimensional Isotropic Heisenberg Models. *Phys. Rev. Lett.* **1966**, *17*, 1133.
(24) Onsager, L. Crystal Statistics. I. A Two-Dimensional Model with an Order-Disorder Transition. *Phys. Rev.* **1944**, *65*, 117−149.
(25) Gonzalez-Herrero, H.; Gomez-Rodriguez, J. M.; Mallet, P.; Moaied, M.; Jose Palacios, J.; Salgado, C.; Ugeda, M. M.; Veuillen, J.-Y.; Yndurain, F.; Brihuega, I. Atomic-Scale Control of Graphene Magnetism by Using Hydrogen Atoms. *Science* **2016**, *352*, 437−441.
(26) Son, Y. W.; Cohen, M. L.; Louie, S. G. Half-Metallic Graphene Nanoribbons. *Nature* **2006**, *444*, 347−349.
(27) Liu, H.; Sun, J.-T.; Fu, H.-X.; Sun, P.-J.; Feng, Y. P.; Meng, S. All-Silicon Switchable Magnetoelectric Effect through Interlayer Exchange Coupling. *ChemPhysChem* **2017**, *18*, 1916−1920.
(28) Cai, L.; He, J.; Liu, Q.; Yao, T.; Chen, L.; Yan, W.; Hu, F.; Jiang, Y.; Zhao, Y.; Hu, T.; et al. Vacancy-Induced Ferromagnetism of MoS_2 Nanosheets. *J. Am. Chem. Soc.* **2015**, *137*, 2622−2627.
(29) Huang, B.; Clark, G.; Navarro-Moratalla, E.; Klein, D. R.; Cheng, R.; Seyler, K. L.; Zhong, D.; Schmidgall, E.; McGuire, M. A.; Cobden, D. H.; et al. Layer-Dependent Ferromagnetism in a van der Waals Crystal Down to the Monolayer Limit. *Nature* **2017**, *546*, 270−273.
(30) Gong, C.; Li, L.; Li, Z.; Ji, H.; Stern, A.; Xia, Y.; Cao, T.; Bao, W.; Wang, C.; Wang, Y.; et al. Discovery of Intrinsic Ferromagnetism in Two-Dimensional van der Waals Crystals. *Nature* **2017**, *546*, 265−269.
(31) Ashton, M.; Paul, J.; Sinnott, S. B.; Hennig, R. G. Topology-Scaling Identification of Layered Solids and Stable Exfoliated 2D Materials. *Phys. Rev. Lett.* **2017**, *118*, 106101.
(32) Mounet, N.; Gibertini, M.; Schwaller, P.; Campi, D.; Merkys, A.; Marrazzo, A.; Sohier, T.; Castelli, I. E.; Cepellotti, A.; Pizzi, G.; et al. Two-Dimensional Materials from High-Throughput Computational Exfoliation of Experimentally Known Compounds. *Nat. Nanotech.* **2018**, *13*, 246−252.
(33) Bjorkman, T.; Gulans, A.; Krasheninnikov, A. V.; Nieminen, R. M. Van Der Waals Bonding in Layered Compounds from Advanced Density-Functional First-Principles Calculations. *Phys. Rev. Lett.* **2012**, *108*, 235502.
(34) Lebègue, S.; Björkman, T.; Klintenberg, M.; Nieminen, R. M.; Eriksson, O. Two-Dimensional Materials from Data Filtering and Ab Initio Calculations. *Phys. Rev. X* **2013**, *3*, 031002.
(35) Rhone, T. D.; Chen, W.; Desai, S.; Yacoby, A.; Kaxiras, E. Data-Driven Studies of Magnetic Two-Dimensional Materials. arXiv:1806.07989 [cond-mat.mtrl-sci] 2018.
(36) Ataca, C.; Şahin, H.; Ciraci, S. Stable, Single-Layer MX_2 Transition-Metal Oxides and Dichalcogenides in a Honeycomb-Like Structure. *J. Phys. Chem. C* **2012**, *116*, 8983−8999.
(37) Rasmussen, F. A.; Thygesen, K. S. Computational 2D Materials Database: Electronic Structure of Transition-Metal Dichalcogenides and Oxides. *J. Phys. Chem. C* **2015**, *119*, 13169−13183.
(38) Hachmann, J.; Olivares-Amaya, R.; Atahan-Evrenk, S.; Amador-Bedolla, C.; Sánchez-Carrera, R. S.; Gold-Parker, A.; Vogt, L.; Brockway, A. M.; Aspuru-Guzik, A. The Harvard Clean Energy Project: Large-Scale Computational Screening and Design of Organic Photovoltaics on the World Community Grid. *J. Phys. Chem. Lett.* **2011**, *2*, 2241−2251.
(39) Li, S.; Chung, Y. G.; Simon, C. M.; Snurr, R. Q. High-Throughput Computational Screening of Multivariate Metal-Organic Frameworks (MTV-MOFs) for CO_2 Capture. *J. Phys. Chem. Lett.* **2017**, *8*, 6135−6141.
(40) Cheng, L.; Assary, R. S.; Qu, X.; Jain, A.; Ong, S. P.; Rajput, N. N.; Persson, K.; Curtiss, L. A. Accelerating Electrolyte Discovery for Energy Storage with High-Throughput Screening. *J. Phys. Chem. Lett.* **2015**, *6*, 283−291.
(41) Gatti, M.; Bruneval, F.; Olevano, V.; Reining, L. Understanding Correlations in Vanadium Dioxide from First Principles. *Phys. Rev. Lett.* **2007**, *99*, 266402.
(42) Eyert, V. VO_2: A Novel View from Band Theory. *Phys. Rev. Lett.* **2011**, *107*, 016401.
(43) Iori, F.; Gatti, M.; Rubio, A. Role of Nonlocal Exchange in the Electronic Structure of Correlated Oxides. *Phys. Rev. B.* **2012**, *85*, 115129.
(44) Yuan, X.; Zhang, Y.; Abtew, T. A.; Zhang, P.; Zhang, W. VO_2: Orbital Competition, Magnetism, and Phase Stability. *Phys. Rev. B* **2012**, *86*, 235103.
(45) Rao, C. N. R. Transition Metal Oxides. *Annu. Rev. Phys. Chem.* **1989**, *40*, 291.
(46) Ashton, M.; Gluhovic, D.; Sinnott, S. B.; Guo, J.; Stewart, D. A.; Hennig, R. G. Two-Dimensional Intrinsic Half-Metals with Large Spin Gaps. *Nano Lett.* **2017**, *17*, 5251−5257.
(47) Liu, J.; Sun, Q.; Kawazoe, Y.; Jena, P. Exfoliating Biocompatible Ferromagnetic Cr-Trihalide Monolayers. *Phys. Chem. Chem. Phys.* **2016**, *18*, 8777−8784.
(48) Chen, P.; Zou, J. Y.; Liu, B. G. Intrinsic Ferromagnetism and Quantum Anomalous Hall Effect in a $CoBr_2$ Monolayer. *Phys. Chem. Chem. Phys.* **2017**, *19*, 13432−13437.
(49) Sarikurt, S.; Kadioglu, Y.; Ersan, F.; Vatansever, E.; Akturk, O. U.; Yuksel, Y.; Akinci, U.; Akturk, E. Electronic and Magnetic Properties of Monolayer α-$RuCl_3$: A First-Principles and Monte Carlo Study. *Phys. Chem. Chem. Phys.* **2018**, *20*, 997−1004.
(50) Huang, C.; Zhou, J.; Wu, H.; Deng, K.; Jena, P.; Kan, E. Quantum Anomalous Hall Effect in Ferromagnetic Transition Metal Halides. *Phys. Rev. B* **2017**, *95*, 045113.
(51) Zhuang, H. L.; Xie, Y.; Kent, P. R. C.; Ganesh, P. Computational Discovery of Ferromagnetic Semiconducting Single-Layer $CrSnTe_3$. *Phys. Rev. B* **2015**, *92*, 035407.
(52) Kurz, P.; Bihlmayer, G.; Blügel, S. Magnetism and Electronic Structure of *hcp* Gd and the Gd(0001) Surface. *J. Phys.: Condens. Matter* **2002**, *14*, 6353.
(53) Hynninen, T.; Raebiger, H.; von Boehm, J.; Ayuela, A. High Curie Temperatures in (Ga,Mn)N from Mn Clustering. *Appl. Phys. Lett.* **2006**, *88*, 122501.
(54) Fuh, H. R.; Chang, C. R.; Wang, Y. K.; Evans, R. F.; Chantrell, R. W.; Jeng, H. T. New type Single-Layer Magnetic Semiconductor in Transition-Metal Dichalcogenides VX_2 (X = S, Se and Te). *Sci. Rep.* **2016**, *6*, 32625.
(55) Turek, I.; Kudrnovský, J.; Bihlmayer, G.; Blügel, S. Ab Initio Theory of Exchange Interactions and the Curie Temperature of Bulk Gd. *J. Phys.: Condens. Matter* **2003**, *15*, 2771.

DOI: 10.1021/acs.jpclett.8b02783
J. Phys. Chem. Lett. 2018, 9, 6709−6715

(56) Strečka, J.; Jaščur, M. A Brief Account of the Ising and Ising-Like Models: Mean-Field, Effective-Field and Exact Results. *Acta Phys. Slovaca* **2015**, *65*, 235.
(57) Zhu, Y.; Kong, X.; Rhone, T. D.; Guo, H. Systematic Search for Two-Dimensional Ferromagnetic Materials. *Phys. Rev. Mater.* **2018**, *2*, No. 081001.
(58) Ono, A.; Ishihara, S. Double-Exchange Interaction in Optically Induced Nonequilibrium State: A Conversion from Ferromagnetic to Antiferromagnetic Structure. *Phys. Rev. Lett.* **2017**, *119*, 207202.
(59) Thielemann-Kühn, N.; Schick, D.; Pontius, N.; Trabant, C.; Mitzner, R.; Holldack, K.; Zabel, H.; Föhlisch, A.; Schüßler-Langeheine, C. Ultrafast and Energy-Efficient Quenching of Spin Order: Antiferromagnetism Beats Ferromagnetism. *Phys. Rev. Lett.* **2017**, *119*, 197202.
(60) Sears, J. A.; Songvilay, M.; Plumb, K. W.; Clancy, J. P.; Qiu, Y.; Zhao, Y.; Parshall, D.; Kim, Y.-J. Magnetic Order in α-$RuCl_3$: A Honeycomb-Lattice Quantum Magnet with Strong Spin-Orbit Coupling. *Phys. Rev. B* **2015**, *91*, 144420.
(61) Kim, H.-S.; V, V. S.; Catuneanu, A.; Kee, H.-Y. Kitaev Magnetism in Honeycomb $RuCl_3$ with Intermediate Spin-Orbit Coupling. *Phys. Rev. B* **2015**, *91*, 241110.
(62) Cao, H. B.; Banerjee, A.; Yan, J. Q.; Bridges, C. A.; Lumsden, M. D.; Mandrus, D. G.; Tennant, D. A.; Chakoumakos, B. C.; Nagler, S. E. Low-Temperature Crystal and Magnetic Structure of α-$RuCl_3$. *Phys. Rev. B* **2016**, *93*, 134423.
(63) Wang, Z.; Reschke, S.; Hüvonen, D.; Do, S. H.; Choi, K. Y.; Gensch, M.; Nagel, U.; Rõõm, T.; Loidl, A. Magnetic Excitations and Continuum of a Possibly Field-Induced Quantum Spin Liquid in α-$RuCl_3$. *Phys. Rev. Lett.* **2017**, *119*, 227202.
(64) Little, A.; Wu, L.; Lampen-Kelley, P.; Banerjee, A.; Patankar, S.; Rees, D.; Bridges, C. A.; Yan, J. Q.; Mandrus, D.; Nagler, S. E.; et al. Antiferromagnetic Resonance and Terahertz Continuum in α-$RuCl_3$. *Phys. Rev. Lett.* **2017**, *119*, 227201.
(65) Yu, Y. J.; Xu, Y.; Ran, K. J.; Ni, J. M.; Huang, Y. Y.; Wang, J. H.; Wen, J. S.; Li, S. Y. Ultralow-Temperature Thermal Conductivity of the Kitaev Honeycomb Magnet α-$RuCl_3$ across the Field-Induced Phase Transition. *Phys. Rev. Lett.* **2018**, *120*, 067202.
(66) Winter, S. M.; Riedl, K.; Kaib, D.; Coldea, R.; Valentí, R. Probing α-$RuCl_3$ Beyond Magnetic Order: Effects of Temperature and Magnetic Field. *Phys. Rev. Lett.* **2018**, *120*, 077203.
(67) Xiao, D.; Chang, M.-C.; Niu, Q. Berry Phase Effects on Electronic Properties. *Rev. Mod. Phys.* **2010**, *82*, 1959−2007.
(68) Xiao, D.; Yao, W.; Niu, Q. Valley-Contrasting Physics in Graphene: Magnetic Moment and Topological Transport. *Phys. Rev. Lett.* **2007**, *99*, 236809.
(69) Crisostomo, C. P.; Huang, Z.-Q.; Hsu, C.-H.; Chuang, F.-C.; Lin, H.; Bansil, A. Chemically Induced Large-Gap Quantum Anomalous Hall Insulator States in III-Bi Honeycombs. *npj Comput. Mater.* **2017**, *3*, 39.
(70) Schliemann, J.; MacDonald, A. H. Noncollinear Ferromagnetism in (III,Mn)V Semiconductors. *Phys. Rev. Lett.* **2002**, *88*, 137201.

DOI: 10.1021/acs.jpclett.8b02783
J. Phys. Chem. Lett. 2018, 9, 6709−6715